CrossMark

Fermi-Large Area Telescope Observations of the Brightest Gamma-Ray Flare Ever Detected from CTA 102

Raj Prince[1] , Gayathri Raman[1], Joachim Hahn[2], Nayantara Gupta[1], and Pratik Majumdar[3]
[1] Raman Research Institute, Sadashivanagar, Bangalore 560080, India; rajprince@rri.res.in
[2] Max-Planck-Institut für Kernphysik, P.O. Box 103980, D-69029 Heidelberg, Germany
[3] Saha Institute of Nuclear Physics, HBNI, Kolkata, West Bengal 700064, India

Abstract

We present a multiwavelength study of the FSRQ CTA 102 using *Fermi*-LAT and simultaneous Swift-XRT/ UVOT observations. The *Fermi*-LAT telescope detected one of the brightest flares from this object during 2016 September to 2017 March. In the 190 days of the observation period, the source underwent four major flares. A detailed analysis of the temporal and spectral properties of these flares indicates the flare at MJD 57751.594 has a γ-ray flux of $(30.12 \pm 4.48) \times 10^{-6}\,\mathrm{ph\,cm^{-2}\,s^{-1}}$ (from 90 minutes binning) in the energy range of 0.1–300 GeV. This has been found to be the highest flux ever detected from CTA 102. Time dependent leptonic modeling of the preflare, rising state, flares and decaying state has been done. A single emission region of size $6.5 \times 10^{16}\,\mathrm{cm}$ has been used in our work to explain the multiwavelength spectral energy distributions. During flares, the luminosity in electrons increases nearly seventy times compared to the preflare state.

Key words: galaxies: active – gamma rays: galaxies – quasars: individual (CTA 102)

1. Introduction

The blazar CTA 102 (FSRQ) is a luminous and well-studied quasar located at a redshift of $z = 1.037$ (Schmidt 1965). Like other blazars, it also has a jet, oriented close to our line of sight. Because of the relativistic beaming effect, all of the emission is beamed along the jet axis and as a result we observe a violent variability at all wavelengths. It was first identified as a quasar by Sandage & Wyndham (1965) and was classified as a highly polarised quasar by Moore & Stockman (1981). It is highly variable in the optical band and its variability has been investigated by Osterman Meyer et al. (2009), who found that faster variability is associated with higher flux states. Due to this behavior, the object has been termed as an Optically Violent Variable quasar (OVV; Maraschi et al. 1986). Variability in the form of flares has also been observed for this source in centimeter and millimeter wavelengths, as well as in the X-rays (*RXTE* observation, Osterman Meyer et al. 2009).

CTA 102 has also been observed in the γ-ray energy band by CGRO/EGRET and *Fermi*-LAT telescopes, where the source luminosity was observed to be $L_\gamma = 5 \times 10^{47}\,\mathrm{erg\,s^{-1}}$; hence, it is listed as a γ-ray bright source (Nolan et al. 1993; Abdo et al. 2009). The Very Large Array observation revealed its kpc-scale radio morphology with a strong central core and two less luminous lobes on opposite sides (Spencer et al. 1989; Stanghellini et al. 1998). The Very Long Baseline Array (VLBA) 2 cm survey and its successor, the MOJAVE (MOnitering of Jets in Active galactic nuclei with VLBA Experiments) program have regularly monitored CTA 102 since mid-1995. The radio flare from CTA 102 that was observed around 2006 was studied by Fromm et al. (2011, 2013a, 2013b). VLBA data collected over a period of 2005 May to 2007 April spanning a frequency range of 2–86 GHz was used to study the physical and kinetic properties of the jet. The apparent speeds of the various regions along the jet were estimated to be in the range of $0.77 \pm 0.14c$ to $13.0 \pm 2.1c$ (Fromm et al. 2013a). The authors concluded that the variation in physical properties during the flare was connected to a new

traveling feature and to the interaction between the shock wave and a stationary structure (Fromm et al. 2013b).

Results from the MOJAVE observations of the source morphology and kinematics at 15 GHz suggest that the apparent speed of the jet between $1.39c$ and $8.64c$ (Lister et al. 2013). VLBA observations at 43 GHz revealed even higher apparent speed of $18c$ (Jorstad et al. 2001, 2005). The variability Doppler factor was estimated to be 22.3 ± 4.5 by Jorstad et al. (2005). Two quasi-stationary components were previously observed by Jorstad et al. (2005) and the five moving components in the jet that were observed by Casadio et al. (2015) N1, N2, N3, N4 and S1 revealed the details of the jet's structure and its kinetic properties. The apparent speeds of the moving components N1, N2, N3 and N4 were reported as $14.9 \pm 0.2c$, $19.4 \pm 0.8c$, $26.9 \pm 1.8c$ and $11.3 \pm 1.2c$ by Casadio et al. (2015), who estimated the corresponding variability Doppler factors of these components as 14.6, 22.4, 26.1, and 30.3, respectively.

Li et al. (2018) recently studied the variability of CTA 102 covering the 2016 January flare. New 15 GHz, archival 43 GHz VLBA data and the variable optical flux density, degree of polarization, electric vector position angle have been used to infer the properties of its jet. Li et al. inferred the Lorentz bulk factor of the jet to be more than 17.5 and intrinsic half opening angle less than $1°8$ from VLBA data.

A prominent flare of flux $F_{>100\mathrm{MeV}} = 5.2 \pm 0.4 \times 10^{-6}\,\mathrm{ph\,cm^{-2}\,s^{-1}}$ (Casadio et al. 2015) was detected by the LAT in 2012 September–October. An optical and near-infrared (NIR) outburst was also simultaneously detected.

They found that the γ-ray outburst was coincident with outbursts in all frequencies and was related to the passage of a new superluminal knot through the radio core. During the flare, the optical polarized emission showed intraday variability.

The late-2016 activity of CTA 102 was associated with intranight variability in optical fluxes (Bachev et al. 2017). The brightest flare from this source has been observed during the late -2016 to early-2017 high state.

Table 1
Table Shows the Log of the Observations Used for This Work

Observatory	Obs-ID	Date (MJD)	Exposure (ks)
Fermi-LAT		57650–−57840	
Swift-XRT	00033509081	57651	1.0
Swift-XRT	00033509082	57657	0.8
Swift-XRT	00033509085	57675	1.0
Swift-XRT	00033509086	57681	1.0
Swift-XRT/UVOT	00033509087	57688	1.9
Swift-XRT/UVOT	00033509088	57689	1.7
Swift-XRT/UVOT	00033509090	57690	1.7
Swift-XRT/UVOT	00033509091	57691	1.6
Swift-XRT/UVOT	00033509092	57692	2.2
Swift-XRT/UVOT	00033509093	57706	2.9
Swift-XRT/UVOT	00033509094	57708	2.7
Swift-XRT/UVOT	00033509095	57710	3.1
Swift-XRT/UVOT	00033509096	57712	2.4
Swift-XRT/UVOT	00033509097	57714	1.7
Swift-XRT/UVOT	00033509098	57715	2.9
Swift-XRT/UVOT	00033509099	57719	1.9
Swift-XRT/UVOT	00033509101	57723	1.3
Swift-XRT/UVOT	00033509103	57728	1.9
Swift-XRT	00033509105	57735	2.6
Swift-XRT/UVOT	00033509106	57738	2.4
Swift-UVOT	00033509107	57740	0.8
Swift-UVOT	00033509108	57742	2.4
Swift-XRT/UVOT	00033509109	57745	2.0
Swift-XRT/UVOT	00033509110	57748	1.6
Swift-XRT/UVOT	00033509111	57751	1.8
Swift-XRT/UVOT	00033509112	57752	1.4
Swift-XRT/UVOT	00088026001	57753	2.0
Swift-XRT/UVOT	00033509114	57754	1.4
Swift-XRT/UVOT	00033509113	57755	1.5
Swift-XRT/UVOT	00033509115	57759	2.4
Swift-XRT/UVOT	00033509116	57761	2.4
Swift-XRT/UVOT	00033509117	57763	2.5
Swift-UVOT	00033509118	57765	0.5
Swift-XRT/UVOT	00033509119	57768	1.0
Swift-XRT/UVOT	00033509120	57771	1.7

In this work, we have studied the high state between 2016 September and 2017 March using γ-ray and X-ray/UVOT data to explore the fast variability and time dependent multi-frequency spectral energy distributions (SEDs).

Unless otherwise mentioned, we adopt the γ-ray flux in units of 10^{-6} ph cm^{-2} s^{-1} throughout this paper. We have used the flat cosmology model with $H_0 = 69.6$ km s^{-1} Mpc^{-1}, and $\Omega_M = 0.27$ to estimate the luminosity distance ($d_L = 7.08 \times 10^9$ pc).

2. Observations and Data Reduction

CTA 102 was observed using *Fermi*-LAT and Swift-XRT/UVOT during 2016 September–2017 March, details of which are given in Table 1.

2.1. Fermi-LAT

Fermi-LAT is a pair conversion γ-ray Telescope that is sensitive to photon energies between 20 MeV to higher than 500 GeV, with a field of view of about 2.4 sr (Atwood et al. 2009). The LAT's field of view covers about 20% of the sky at any time, and it scans the whole sky every three hours. The instrument was launched by NASA in 2008 into a

near-Earth orbit CTA 102 has been continuously monitored by *Fermi*-LAT since 2008 August. The first flare of CTA 102 was observed in 2012 September–October, with a highest flux of 5.2 ± 0.4 (Casadio et al. 2015). The second flare observed during 2016 September–2017 March is brighter than the first. We have analyzed the *Fermi*-LAT data from 2016 September 19 to 2017 March 31 (MJD 57650-57840) to study this flare. The standard data reduction and analysis procedure[4] has been followed. The *gtlike/pyLikelihood* method is used to analyze the data, which is part of the latest version (v10r0p5) of *Fermi Science Tools*. The present analysis has been carried out after rejecting events with a zenith angle >90° to reduce the contamination from the Earth's limb γ-rays. The latest Instrument Response Function "P8R2_SOURCE_V6" has been used in the analysis. The photons are extracted from a circular region of radius 10°, with the region of interest (ROI) centered at the position of CTA 102. The third *Fermi*-LAT catalog (3FGL; Acero et al. 2015) has been used to include the sources lying within a radius of 10°. All of the spectral and flux parameters of the sources lying within 10° from the center of ROI are left free to vary during model fitting. The model file also includes the sources within 10°–20° from the center of ROI. However, all of their spectral and flux parameters are kept fixed to the 3FGL catalog values. This also includes the latest isotropic background model, "iso_P8R2_SOURCE_V6_v06", and the galactic diffuse emission model, "gll_iem_v06", both of which are standard models that are available from the *Fermi* Science Support Center[5] (FSSC). A maximum likelihood (ML) test has been done to test the significance of the γ-ray signal. The ML is defined as TS = 2Δ log(L), where L is the likelihood function between models with and without a point source at the position of the source of interest (Paliya 2015). The ML analysis was performed over the period of our interest and the sources which fall below 3σ detection limit (i.e., TS < 9; for details see Mattox et al. 1996) are removed from the model file.

The spectral properties of the *Fermi*-LAT detected blazars are most often studied by fitting their differential gamma-ray spectrum with the following functional forms (Abdo et al. 2010a):

1. A power law (PL), defined as

$$dN(E)\big/dE = N_0(E/E_p)^{-\Gamma}, \qquad (1)$$

with pivot energy (energy at which error on differential flux is minimal) $E_p = 476.0$ MeV from 1FGL (Abdo et al. 2010b).

2. A log-parabola (LP), defined as

$$dN(E)/dE = N_0(E/E_0)^{-\alpha - \beta \ln(E/E_0)}, \qquad (2)$$

with pivot energy $E_0 = 308.3$ MeV from 3FGL (Acero et al. 2015), where α is the photon index at E_0, β is the curvature index and "ln" is the natural logarithm.

3. A PL with an exponential cut-off (PLEC), defined as

$$dN(E)\big/dE = N_0(E/E_p)^{-\Gamma}\exp(-E/E_c), \qquad (3)$$

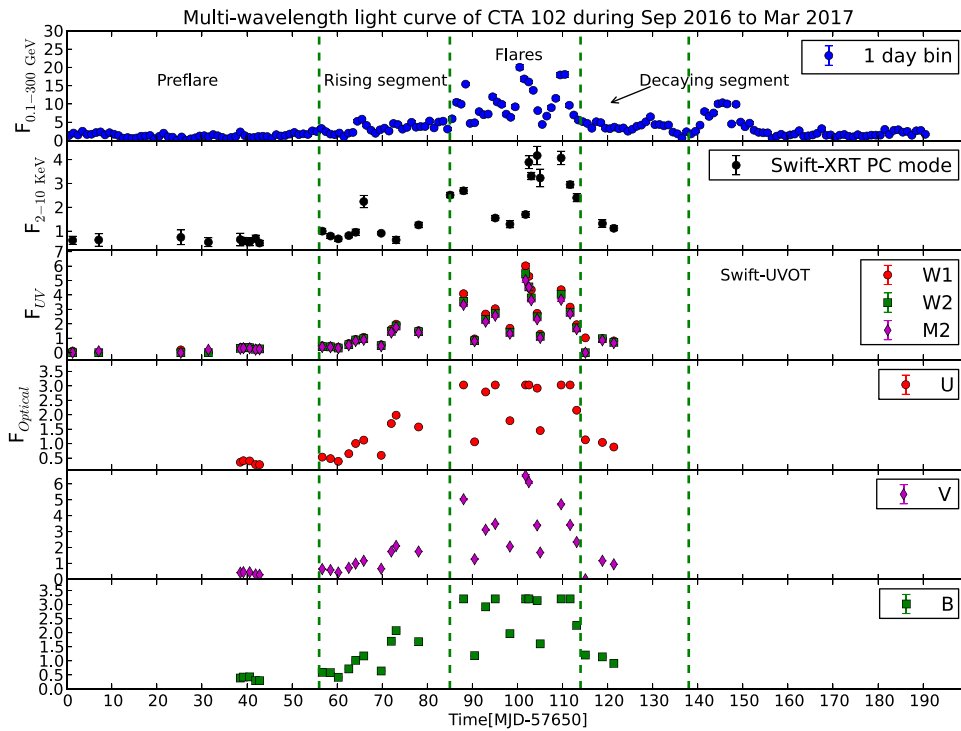with pivot energy $E_p = 476.0$ MeV from 1FGL (Abdo et al. 2010b).

Figure 1. Light curve of the CTA 102 during the 2016 September–2017 March outburst. Four major flaring episodes have been identified and further studied. Preflare, rising and decaying segments are also present before and after the flaring episodes, separated by a green dashed line. XRT is in unit of 10^{-11}, F_{UV} and $F_{optical}$ is in unit of 10^{-10} erg cm^{-2} s^{-1}. γ-ray flux shown in the top panel is in unit of 10^{-6} ph cm^{-2} s^{-1}.

4. A broken PL (BPL), defined as

$$dN(E)/dE = N_0(E/E_{break})^{-\Gamma_i}, \qquad (4)$$

with $i = 1$ if $E < E_{break}$ and $i = 2$ if $E > E_{break}$.

2.2. Swift-XRT and UVOT

CTA 102 was observed by Swift-XRT/UVOT during the flaring period of 2016 September–2017 January (there was no observation during 2017 February and March). The details of the observations are presented in Table 1.

Cleaned event files were obtained using the task *xrtpipeline,* version 0.13.2. The latest calibration files (CALDB version 20160609) and standard screening criteria were used to re-process the raw data. Cleaned event files corresponding to the Photon Counting mode were considered. Circular regions of radius 25 arcsec centered at the source and slightly away from the source were chosen for the source and the background regions, respectively, while analyzing the XRT data.

The X-ray spectra were extracted in *xselect*. The *xrtmkarf* tool was used to produce the ancillary response file and *grppha* was used to group the spectra to obtain a minimum of 30 counts per bin. The grouped spectra were loaded in XSPEC for spectral fitting. All of the spectra were fitted using an absorbed BPL model with a galactic absorption column density of $n_H = 5.0 \times 10^{20}$ cm^{-2} (Kalberla et al. 2005).

The Swift Ultraviolet/Optical Telescope (UVOT, Roming et al. 2005) also observed CTA 102 in all six filters: U, V, B, W1, M2 and W2. The source image was extracted from a region of 10 arcsec centered at the source. The background region was chosen with a radius of 30 arcsec away from the source from a nearby source free region. The uvotsource task has been used to extract the source magnitudes and fluxes. The magnitudes are corrected for galactic extinction (Schlafly &

Finkbeiner 2011) and converted into flux using the zero points (Breeveld et al. 2011) and conversion factors (Larionov et al. 2016).

3. Results

Our results on the light curves, variability time, and spectral analysis during the 2016 September–2017 March flaring period of CTA 102 are presented in this section.

3.1. Light Curves—Gamma Ray

The variability of the source can be determined from its light curve. The light curve of CTA 102, observed by the *Fermi*-LAT during 2016 September–2017 March, has been shown in the top panel of Figure 1. The γ-ray variability of the source can be clearly seen by generating the light curves (see Figure 2) with various time bins (1 day, 12, 6, and 3 hr). The spectral analysis has been carried out using the *unbinned likelihood analysis* method over several periods of flaring states in the energy range of 0.1–300 GeV. The whole light curve is divided into four parts: preflare, rising segment, flare and decaying segment (which are separated by green dotted lines). The source started showing high activity during MJD 57735 and went on till MJD 57763 (Figure 2). The flaring state lasted for 28 days and is divided into four flares. These four flares are separated by dotted red lines in Figure 2. We have named them flare-1, flare-2, flare-3 and flare-4, which corresponds to MJD 57735–57740, MJD 57740–57748, MJD 57748–57756 and MJD 57756–57763, respectively. The quiescent states before and after the flaring period are identified as preflare phase, rising segment and decaying segment, respectively. The various time bins (1 day, 12, 6 and 3 hr) are applied to study the behavior of CTA 102 during the flaring period. In Figure 2, the light curves for different time bins are shown in different
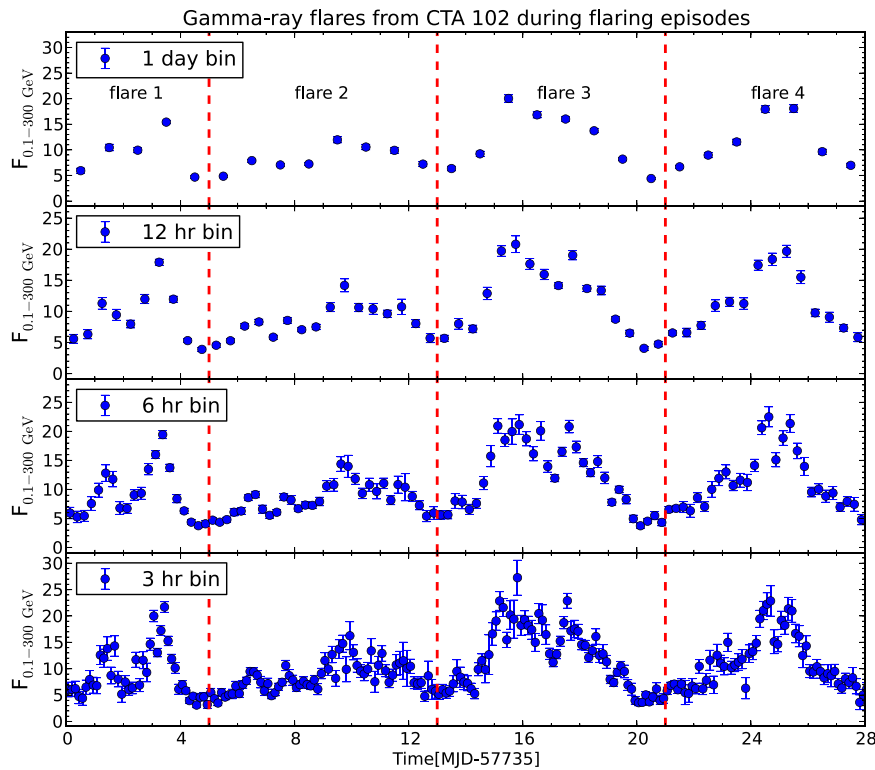
Figure 2. Zoomed version of flaring episodes. The flares are separated by red dashed lines and their time durations are as follows: MJD 57735–57740, MJD 57740–57748, MJD 57748–57756, and MJD 57756–57763. Substructures are clearly seen from 6 and 3 hr binning which also hints about the flux variability shorter than day scale.

panels. The top panel represents 1 day time binning, which reveals the four flares. The 12, 6 and 3 hr binning reveals the substructures in each flare. These substructures are nothing but the collection of peaks of different heights. The data points shown in the bottom most panel (i.e., 3 hr binning) of Figure 2 are used to study the variability timescale and the data points in the panel just above it (i.e., 6 hr binning) are used to study the temporal behavior. The data points below the detection limit of 3σ (TS < 9; Mattox et al. 1996) have been rejected from both the temporal and variability study.

The temporal evolution of each flare has been studied separately. For this purpose, we have fitted the peaks that are found in the 6 hr binning of light curve by a sum of exponentials, which gives the rise and decay times of each peak. The functional form of the sum of exponentials is as follows:

$$F(t) = 2F_0 \left[\exp\left(\frac{t_0 - t}{T_r} \right) + \exp\left(\frac{t - t_0}{T_d} \right) \right]^{-1}, \quad (5)$$

where F_0 is the flux at time t_0 representing the approximate flare amplitude, T_r and T_d are the rise and decay times of the flare, respectively (Abdo et al. 2010c).

Any physical process faster than the light travel time or the duration of the event will not be detectable from the light curve (Chiaberge & Ghisellini 1999; Chatterjee et al. 2012). A symmetric temporal evolution, with equal rise and decay times, may occur when a perturbation in the jet flow or a blob of denser plasma passes through a standing shock present in the jet (Blandford & Königl 1979). In flare-1, the first peak (P1) has nearly equal rise and decay times, while the second peak (P2) has a longer rise time than decay time. This could be due

to slow injection of electrons into the emission region. This is also seen in first peak (P1) and fourth peak (P4) of flare-2. A slower decay time could be due to longer cooling time of electrons. In flare-2, the second peak (P2) and in flare-3 the fourth peak (P4) have a significantly longer decay time than rise time. Among the 14 peaks of four flares given in Table 2, five peaks have nearly equal rise and decay times. Five peaks have a slower rise time than decay time and the other four have a slower decay time than rise time. Hence, all three scenarios are almost equally probable.

3.1.1. Preflare, Rising and Decaying Segment

Prior to its flaring activity in 2016 December, CTA 102 was in quiescent state, we call this a preflare phase. We have defined the preflare during MJD 57650–MJD 57706 (Figure 1). The average flux during preflare phase is observed to be $F_{GeV} = 1.40 \pm 0.10$ ph cm^{-2} s^{-1}. Just after the MJD 57706, the source flux started rising but very slowly. We call this the rising segment with average flux $F_{GeV} = 3.83 \pm 0.08$ ph cm^{-2} s^{-1}, lasting for a period of one month MJD 57706–MJD 57735. The flaring phase started from MJD 57735 and consisted of four major flares that lasted up to 28 days (till MJD 57763), after which the emission started decaying very slowly. We name this the decaying segment. The average flux in this period was almost similar to the rising segment. In the following sections, we discuss these four flares in detail.

3.1.2. Flare-1

Flare-1, as shown in Figure 2, was observed during MJD 55735–57740, before which the source was in rising state as mentioned in Section 3.1.1. The temporal evolution of flare-1 is
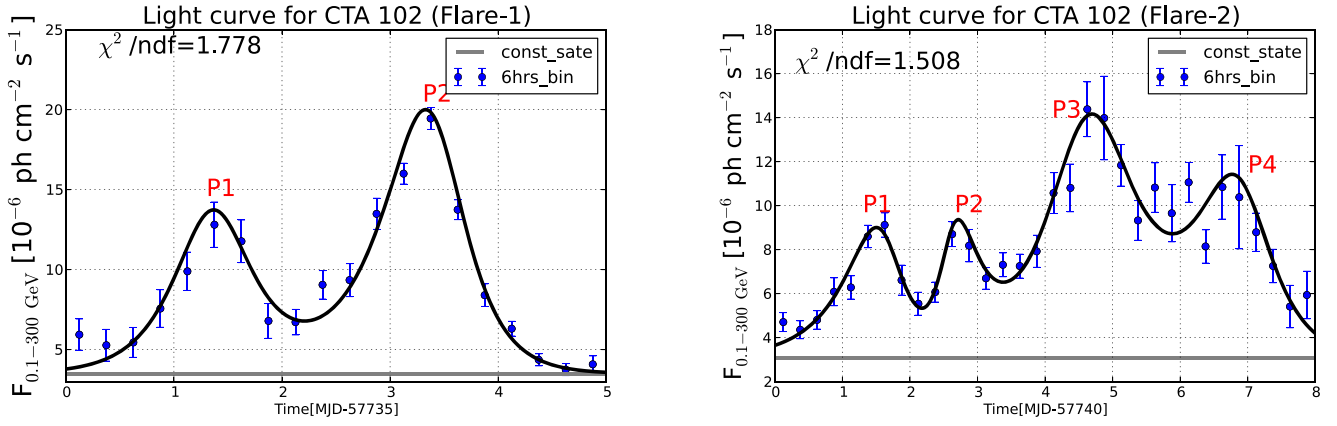
Figure 3. Left-hand panel: light curve of flare-1. Right-hand panel: light curve of flare-2. The peaks of both the flares are fitted by the sum of exponentials and the fitted parameters are mentioned in Table 2. The light gray line represents the constant flux or baseline.

Table 2
Results of Temporal Fitting with Sum of Exponentials (Equation (5) in the Text) for Different Peaks of the Flares

Peak	t_0 (MJD)	F_0 (10^{-6} ph cm^{-2} s^{-1})	T_r (hr)	T_d (hr)
		flare-1		
P1	57736.4	12.81 ± 1.42	7.66 ± 1.35	7.76 ± 1.36
P2	57738.4	19.45 ± 0.68	10.01 ± 0.92	6.51 ± 0.59
		flare-2		
P1	57741.6	9.12 ± 0.55	13.21 ± 2.45	6.31 ± 1.70
P2	57742.6	8.70 ± 0.56	4.01 ± 1.15	9.48 ± 2.11
P3	57744.6	14.38 ± 1.24	12.50 ± 1.84	15.30 ± 3.35
P4	57746.6	10.84 ± 1.46	14.53 ± 4.37	9.83 ± 2.09
		flare-3		
P1	57750.1	20.93 ± 1.24	7.20 ± 1.00	7.45 ± 1.91
P2	57750.9	21.17 ± 1.67	5.61 ± 1.62	6.06 ± 1.84
P3	57751.6	20.09 ± 1.60	4.64 ± 1.61	4.56 ± 0.95
P4	57752.6	20.82 ± 1.08	5.05 ± 0.85	11.41 ± 1.50
P5	57753.6	14.79 ± 1.01	4.94 ± 1.41	4.49 ± 1.17
		flare-4		
P1	57758.1	13.01 ± 1.20	7.21 ± 1.66	4.89 ± 1.41
P2	57759.6	22.50 ± 1.73	10.07 ± 1.36	1.74 ± 0.99
P3	57760.4	21.36 ± 1.52	8.97 ± 1.21	8.72 ± 0.82

Note. Column 2 represents the time (in MJD) at which the peaks were observed and the peak fluxes are given in column 3. The fitted rise (T_r) and decay (T_d) times are given in columns 4 and 5.

shown in the left-hand panel of Figure 3. The 6 hr bins clearly reveal that the flux started rising just from MJD 55735 and lasted up to five days (till MJD 57740). There are two major peaks P1 and P2, during flare-1, at MJD 57736.375 and MJD 57738.375 with a flux of $F_{GeV} = 12.81 \pm 1.42$ and 19.45 ± 0.68 respectively. These peaks are fitted with the function given in Equation (5). The rise and decay times of the peaks are found from this fit. The details of the fitted

parameters are presented in Table 2. This has been done for all the four flares. Along with the peaks we have also fitted the baseline flux, shown in Figure 3 (gray line), which is very close to the quiescent state mentioned in Section 3.1.1.

3.1.3. Flare-2

The temporal evolution of flare-2 (MJD 57740–57748) is shown in the right-hand panel of Figure 3. As flare-1 started to decay at MJD 55740, flare-2 started to rise and lasted up to eight days till MJD 57748. The flaring period of eight days can be clearly divided into four major peaks (Figure 3) called as P1, P2, P3 and P4 which happened at MJD 57741.625, 57742.625, 57744.625 and 57746.625 with a flux of $F_{GeV} = 9.12 \pm 0.55$, 8.70 ± 0.56, 14.38 ± 1.24 and 10.84 ± 1.46 respectively. The baseline flux shown in Figure 3 (gray line) is close to the quiescent state flux.

3.1.4. Flare-3

Similar to flare-1 and flare-2 a 6 hr binning of flare-3 has been done to study the temporal evolution, as shown in left-hand panel of Figure 4. Flare-3 was observed during MJD 57748–57756 and is one of the brightest flares ever detected from CTA 102 with a flux of $F_{GeV} = 27.26 \pm 3.30$ at MJD 57750.813 (from 3 hr binning). It is much brighter than the flare observed in 2012 September–October (Casadio et al. 2015) with a flux of $F_{GeV} = 5.2 \pm 0.4$. The flux started to rise from the point where flare-2 diminished, i.e., at MJD 57748. The source spent around seven days in its flaring state (see Figure 4) subsequently its flux reduced to the quiescent state flux value. The flaring period is divided into five major and clear peaks shown in left-hand panel of Figure 4. The peaks P1, P2, P3, P4 and P5 were observed at MJD 57750.125, 57750.875, 57751.625, 57752.625 and MJD 57753.625 with fluxes of $F_{GeV} = 20.93 \pm 1.24$, 21.17 ± 1.67, 20.09 ± 1.60, 20.82 ± 1.08 and 14.79 ± 1.01 respectively.

3.1.5. Flare-4

A 6 hr binning of flare-4 has also been carried out during MJD 57756–57763 to study the temporal evolution. The light curve of flare-4 is shown in the right-hand panel of Figure 4. The flux started to rise at MJD 57757 and it stayed in the flaring state for around six days (MJD 57757–57763). Three major peaks were observed during the flaring period of flare-4,
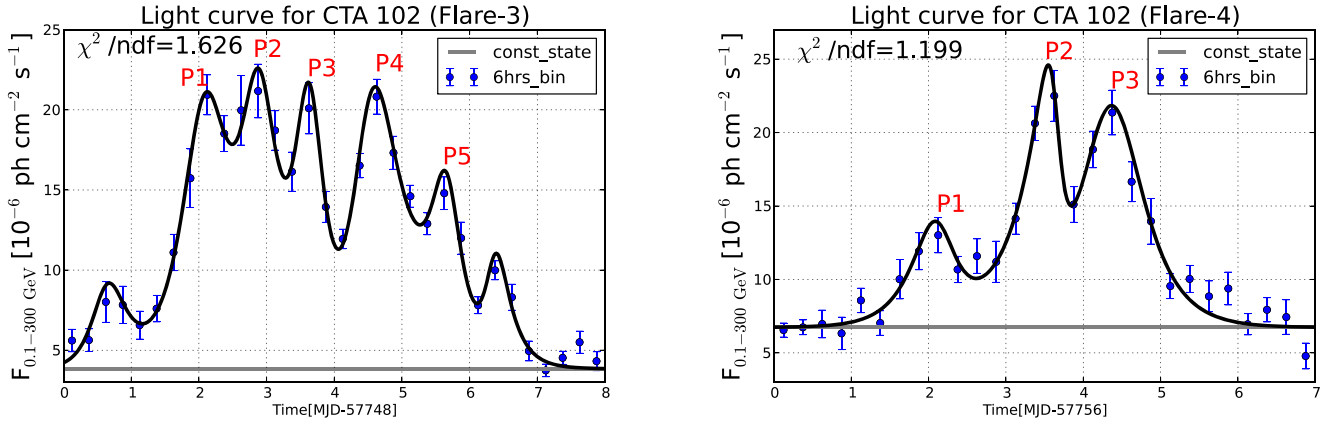
Figure 4. Left-hand panel: light curve of flare-3. Right-hand panel: light curve of flare-4. The peaks of both the flares are fitted by the sum of exponentials and the fitted parameters are mentioned in Table 2. The light gray line represents the constant flux or baseline.

which we name P1, P2, and P3 and which happened at MJD 57758.125, 57759.625, 57760.375 with the fluxes of $F_{\rm GeV} = 13.01 \pm 1.20$, 22.50 ± 1.73, and 21.36 ± 1.52, respectively.

3.2. X-Ray and UV/Optical Light Curves

The simultaneous X-ray (2–10 keV) and UVOT (six filters) light curves are shown in the lower panel of Figure 1. Swift observation for flaring episode was carried out along with *Fermi*-LAT till MJD 57771 (2017 March 18). The 2–10 keV X-ray fluxes that were obtained using the CFLUX convolution model have been used to plot the X-ray light curve in Figure 1. The UVOT light curves show the fluxes in all the six filter bands during each of the observations. The light curves, although sparsely populated when compared to the γ-ray light curves, do show correlated increased intensities during the flaring episodes.

3.3. Variability

The variability time is a measure of how fast the flux is changing with time during the flaring period. It also provides an estimate of the size of the emission region for a given value of Doppler factor (δ) of the jet and redshift (z) of the source. To estimate the fastest variability time, we have done 90 minutes time binning and used the following function:

$$F(t_2) = F(t_1).2^{(t_2-t_1)/t_d}, \qquad (6)$$

where $F(t_1)$ and $F(t_2)$ are the fluxes measured at two instants of time t_1 and t_2, respectively, and t_d represents the doubling/halving timescale of flux. We have scanned all four flares shown in Figure 2 with the function given in Equation (6). While scanning the light curves we use the following conditions: Only those consecutive time instants will be considered which have at least 5σ detection (TS > 25) and the flux between these two time instants should be double (rising part) or half (decaying part). There are time instants that have 5σ detection but the difference in values of fluxes measured at these instants is less than a factor of two, or vice versa. These time instants are completely ignored in our fastest variability analysis. The shortest variability time is found to be $t_{\rm var} = 1.08 \pm 0.01$ hr between MJD 57761.47–57761.53, which is consistent with the hour scale variability found for other FSRQ like PKS 1510-089 (Prince et al. 2017). We also found

that the variability time during flares in *Fermi*-LAT data varies in the range of 1 hr to several days.

3.4. Fractional Variability (F_{var})

Fractional variability is used to determine the variability amplitudes across the whole electromagnetic spectrum (Vaughan et al. 2003) during simultaneous multiwavelength observations of blazars. However, here we have calculated with only the gamma-ray data to identify the different activity states of the blazar. The fractional variability amplitude was first introduced by Edelson & Malkan (1987) and Edelson et al. (1990), and it can be estimated by using the relation given in Vaughan et al. (2003),

$$F_{\rm var} = \sqrt{\frac{S^2 - \sigma^2}{r^2}}, \qquad (7)$$

$$\mathrm{err}(F_{\rm var}) = \sqrt{\left(\sqrt{\frac{1}{2N}} \cdot \frac{\sigma^2}{r^2 F_{\rm var}}\right)^2 + \left(\sqrt{\frac{\sigma^2}{N}} \cdot \frac{1}{r}\right)^2}, \qquad (8)$$

where $\sigma_{XS}^2 = S^2 - \sigma^2$ is called excess variance, S^2 is the sample variance, σ^2 is the mean square uncertainties of each observations and r is the sample mean. We have also estimated the normalized excess variance, $\sigma_{NXS}^2 = \sigma_{XS}^2/r^2$.

The rise in the values of the fractional variability and excess variance from preflare to flare state and subsequent fall during decaying state are shown in Table 3. The fractional variabilities in multiwavelength data have been calculated by Kaur & Baliyan (2018) for the same source, who found larger fractional variability at higher energy e.g., 0.87 in γ-rays, 0.45 in X-rays, 0.082 in UVW2-band and 0.059 in optical *B*-band. Similar
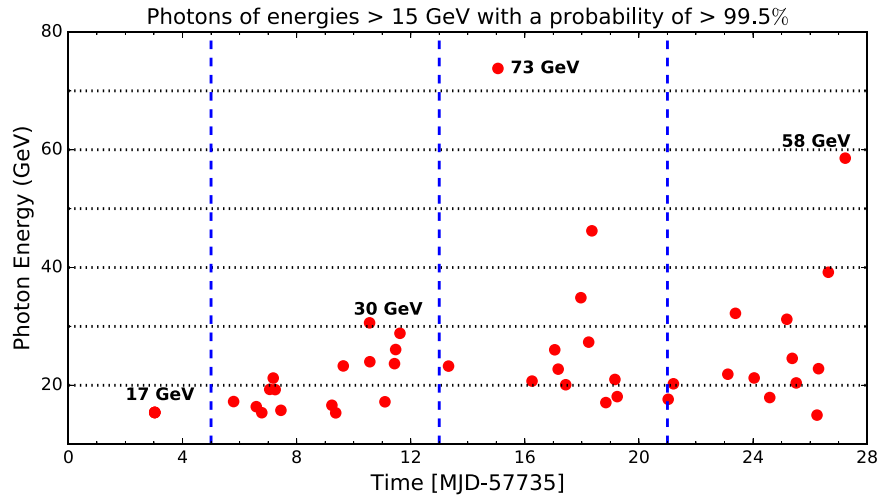
Table 3
Fractional Variability Calculated for All of the Phases (Preflare, Rising Segment, Decaying Segment, and Flare)

Activity	σ_{NXS}^2	$\mathrm{err}(\sigma_{NXS}^2)$	$F_{\rm var}$	$\mathrm{err}(F_{\rm var})$
Preflare	0.0626	0.0192	0.2502	0.0384
Rising segment	0.1295	0.0147	0.3598	0.0205
Decaying segment	0.1189	0.0129	0.3449	0.0188
Flare-(1–4)	0.1899	0.0076	0.4358	0.0087

Figure 5. Arrival time and energy of E > 15 GeV photons, with probability greater than 99.5%, plotted for all the flares. Vertical dashed blue lines are separating the flares.

results have also been reported by Patel et al. (2018) for 1ES 1959 + 650, who found fractional variability increases with increasing energy. The opposite scenario was observed by Bonning et al. (2009) for 3C 454.3, where fractional variability decreases with increasing energy (IR, Optical, UV) due to the presence of steady thermal emission from the accretion disk.

3.5. High Energy Photons

In Figure 5, we plot the photons' energy (>15 GeV) with respect to their arrival time on x-axis for all of the flares shown in Figure 2. To get high energy photons, the *Fermi*-analysis has been done with the ULTRACLEAN class of events and 0°.5 of ROI. The high energy photons that have energy $E > 15$ GeV and also the probability above 99.5% are only presented in Figure 5. We find that a photon of energy $E = 73.8$ GeV was detected at MJD 57750.06 with a probability of 99.99%. This is part of the brightest flare ever detected from CTA 102; i.e., flare-3. This is also the highest energy photon ever detected from CTA 102. Figure 5 reveals that most of the high energy photons are detected during flare-2, 3, and 4. Photons of energy 17, 30 and 58 GeV with probability of 99.99% also have been detected during flare-1, 2 and 4 at MJD 57740.79, 57745.56 and 57762.23, respectively. These high energy photons can be produced in external Compton scattering of the broad line region (BLR), disk or dusty torus photons by the relativistic electrons in the jet and also by synchrotron self-Compton emission.

3.6. Spectral Energy Distributions of Flares

In this section we have focused on the details of the γ-ray SEDs of 2016 September–2017 March flares. From the analysis, we have found the four flares accompanied by quiescent state (i.e., preflare), rising and decaying segments before and after the flaring period. We have performed the spectral analysis of these phases separately. Four different functions (PL, LP, PLEC and BPL) as defined by Equations (1)–(4) have been used to fit the spectral data points using the likelihood analysis. The selection of these functional forms is motivated by earlier studies on spectral analysis of blazar flares (Ackermann et al. 2010). Along with the fitting parameters, the likelihood analysis also returns the Log (likelihood) value, which tells us about the quality of the

unbinned fit. The spectral analysis for all the phases are shown in Figure 6 and their corresponding fitted parameters are presented in Table 4. The photon flux increases drastically during flares. Moreover, significant spectral hardening is present in the photon spectra from flares. Flare-3 had the highest photon flux associated with maximum hardening in the spectrum. Similar features were also noted earlier from flares of other AGN like 3C 454.3 (Britto et al. 2016). The spectral curvature has been identified with the TS_{curve}, which is defined as $TS_{curve} = 2(\log \ \mathcal{L}(LP/PLEC/BPL) - \log \mathcal{L}(PL))$ (Nolan et al. 2012). The spectral curvature is significant if $TS_{curve} > 16$ (Acero et al. 2015). From the parameter values mentioned in Table 4, the maximum curvature in the γ-ray spectra has been noticed during rising, flaring and decaying states.

The *Fermi*-LAT data from preflare is best fitted by a BPL or a LP function. The TS_{curve} values do not differ much in these two cases. The rising segment is best fitted by a LP function. Other than flare-1 which gives a best fit to PLEC, all the three flares and the decaying segment are also best fitted by the LP function. Flare-1 has comparable TS_{curve} values for PLEC and BPL functions. We infer from these results that the observed curvature in the gamma-ray spectra during preflare, rising, flare and decaying states could be due to the curvature in the spectrum of the relativistic electrons in the emission region.

3.7. Modeling the SEDs

We used the publicly available time dependent code GAMERA[6] (Hahn 2015) to model SEDs from astrophysical objects. It solves the time dependent continuity equation to calculate the propagated electron spectrum. The synchrotron and inverse Compton emissions for that electron spectrum are subsequently calculated. We have assumed a spherical emission region or blob moving relativistically to model the jet emission.

In Table 5, our results of spectral fitting are displayed for the preflare, rising, flare and decaying states. In most cases, the LP function gives the best fit to the *Fermi*-LAT data. A LP photon spectrum can be produced by radiative losses of a LP electron spectrum. The injected electron spectrum $Q(E, t)$ could be a LP spectrum (Massaro et al. 2004) if the probability of acceleration
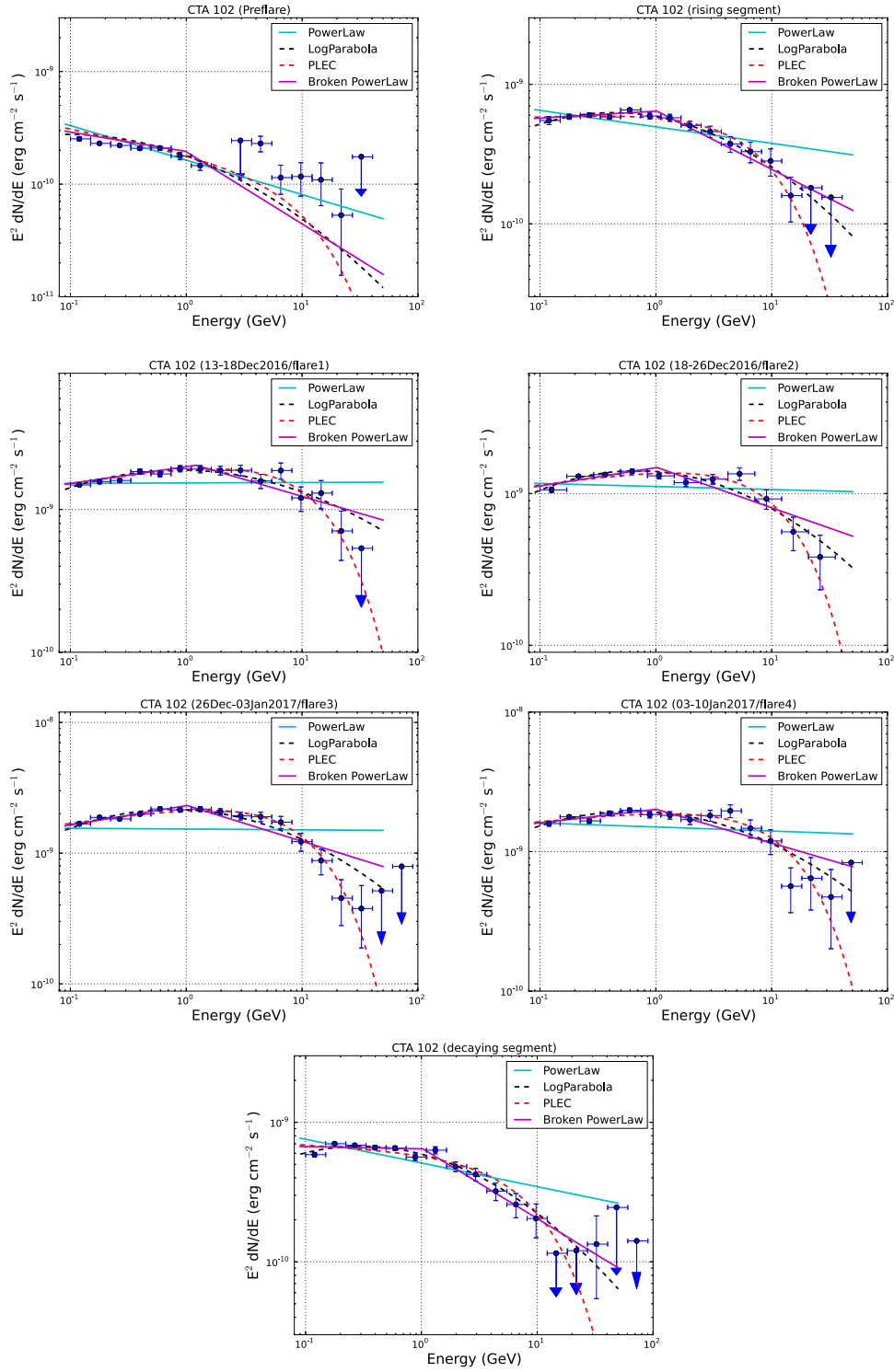
---

6 http://joachimhahn.github.io/GAMERA

Figure 6. *Fermi*-LAT SEDs during the different activity periods shown in Figure 1. The data points are fitted with four different functional forms PL, LP, PLEC, and BPL shown in cyan, black, red, and magenta, respectively. The fitted parameter values are displayed in Table 4.

decreases with increasing energy. This electron spectrum becomes steeper after undergoing radiative losses, which we denote in the following by $N(E, t)$.

The continuity equation for the electron spectrum in our study is

$$\frac{\partial N(E, t)}{\partial t} = Q(E, t) - \frac{\partial}{\partial E}(b(E, t)N(E, t)). \quad (9)$$

The energy loss rate of electrons due to synchrotron, synchrotron self-Compton and external Compton emission has been denoted by $b(E, t)$. GAMERA code calculates the inverse Compton emission using the full Klein–Nishina cross-section from Blumenthal & Gould (1970).

We have not included diffusive loss because it is assumed to be insignificant compared to the radiative losses by the electrons. The photons emitted from the BLR are the targets

Table 4
Results of SEDs Fitted with Different Spectral Distributions PL, LP, PLEC, and BPL

Activity	$F_{0.1–300\,GeV}$ (10^{-6} ph cm^{-2} s^{-1})	PowerLaw (PL) Γ			TS	
Preflare	1.44 ± 0.04	2.31 ± 0.02	⋯		6965.29	⋯
Rising segment	3.87 ± 0.07	2.12 ± 0.01	⋯		18236.04	⋯
Flare-1	10.60 ± 0.17	1.99 ± 0.01	⋯		26338.38	⋯
Flare-2	7.87 ± 0.12	2.02 ± 0.01	⋯		30981.15	⋯
Flare-3	11.90 ± 0.14	2.01 ± 0.01	⋯		46205.62	⋯
Flare-4	11.10 ± 0.18	2.03 ± 0.01	⋯		24250.71	⋯
Decaying segment	4.17 ± 0.07	2.17 ± 0.01	⋯		18320.72	⋯
Activity	$F_{0.1–300\,GeV}$ (10^{-6} ph cm^{-2} s^{-1})	LogParabola (LP) α	β		TS	TS$_{curve}$
Preflare	1.38 ± 0.04	2.18 ± 0.03	0.08 ± 0.02		6980.74	15.45
Rising segment	3.66 ± 0.07	1.96 ± 0.02	0.09 ± 0.01		18333.51	97.47
Flare-1	10.30 ± 0.17	1.87 ± 0.02	0.06 ± 0.01		26408.49	70.11
Flare-2	7.60 ± 0.12	1.87 ± 0.02	0.08 ± 0.01		31083.27	102.12
Flare-3	11.50 ± 0.14	1.85 ± 0.02	0.08 ± 0.01		46437.84	232.22
Flare-4	10.70 ± 0.19	1.89 ± 0.02	0.07 ± 0.01		24332.05	81.34
Decaying segment	3.96 ± 0.07	2.01 ± 0.02	0.09 ± 0.01		18412.52	91.80
Activity	$F_{0.1–300\,GeV}$ (10^{-6} ph cm^{-2} s^{-1})	PLExpCutoff (PLEC) Γ_{PLEC}	E_{cutoff} (GeV)		TS	TS$_{curve}$
Preflare	1.40 ± 0.04	2.21 ± 0.04	12.39 ± 4.16		6976.88	11.59
Rising segment	3.72 ± 0.07	1.97 ± 0.02	9.45 ± 1.46		18326.98	90.94
Flare-1	10.40 ± 0.17	1.88 ± 0.02	14.21 ± 2.22		26421.66	83.28
Flare-2	7.67 ± 0.12	1.89 ± 0.02	12.71 ± 1.79		31081.92	100.77
Flare-3	11.60 ± 0.14	1.87 ± 0.02	11.98 ± 1.33		46414.40	208.78
Flare-4	10.80 ± 0.18	1.92 ± 0.02	15.46 ± 2.69		24326.29	75.58
Decaying segment	4.05 ± 0.07	2.05 ± 0.02	10.76 ± 2.13		18385.50	64.78
Activity	$F_{0.1–300\,GeV}$ (10^{-6} ph cm^{-2} s^{-1})	Broken PowerLaw (BPL) Γ_1	Γ_2	E_{break} (GeV)	TS	TS$_{curve}$
Preflare	1.38 ± 0.06	2.17 ± 0.07	2.64 ± 0.10	0.98 ± 0.12	6984.17	18.88
Rising segment	3.69 ± 0.09	1.96 ± 0.03	2.42 ± 0.05	1.02 ± 0.09	18323.99	87.95
Flare-1	10.40 ± 0.17	1.88 ± 0.02	2.24 ± 0.04	1.21 ± 0.11	26396.25	57.87
Flare-2	7.65 ± 0.12	1.88 ± 0.02	2.27 ± 0.03	1.02 ± 0.04	31060.34	79.19
Flare-3	11.60 ± 0.14	1.85 ± 0.02	2.28 ± 0.03	1.01 ± 0.14	46402.10	196.48
Flare-4	10.80 ± 0.18	1.90 ± 0.03	2.24 ± 0.04	1.01 ± 0.19	24312.09	61.38
Decaying segment	4.00 ± 0.07	2.02 ± 0.03	2.51 ± 0.06	1.03 ± 0.14	18403.22	82.50

Note. The different states during the observations are mentioned in column 1. The values of the fitted fluxes and spectral indices are presented in columns 2 and 3. TS$_{curve}$ = 2(log $\mathcal{L}$(LP/PLEC/BPL) − log $\mathcal{L}$(PL)).

for external Compton emission. BLR photon density in the comoving/jet frame of Lorentz factor Γ is

$$U'_{BLR} = \frac{\Gamma^2 \eta_{BLR} L_{disk}}{4\pi c R_{BLR}^2} \qquad (10)$$

where the photon energy density in BLR is only a fraction $\eta_{BLR} \sim 0.02(2\%)$ of the disc photon energy density. The BLR size is important to estimate the BLR energy density and the absorption of γ-ray from the emission region. The accretion disk luminosity $L_{disk} = 3.8 \times 10^{46}$ erg s^{-1}, central black hole mass $M_{BH} \sim 8.5 \times 10^8 M_\odot$ and Eddington luminosity $L_{Edd} = 1.1 \times 10^{47}$ erg s^{-1} are estimated by Zamaninasab & Clausen-Brown et al. (2014). We have used their estimated value of L_{disk} and $\Gamma = 15$ to calculate U'_{BLR}. We have assumed the radius of the BLR region to be $R_{BLR} = 6.7 \times 10^{17}$ cm following Pian et al. (2005).

The accretion disk emission is also included in estimating the external Compton emission by the relativistic electrons in the jet. The energy density in the comoving frame (Dermer & Menon 2009) is calculated from the following equation

$$U'_{disk} = \frac{0.207 R_g l_{Edd} L_{Edd}}{\pi c z^3 \Gamma^2}. \qquad (11)$$

The gravitational radius is denoted by R_g, the Eddington ratio by $l_{Edd} = L_{disk}/L_{Edd}$ and $z = 6.7 \times 10^{17}$ cm is the distance of the emission region from the black hole. The accretion disk temperature is estimated from Dermer & Menon (2009) by using the l_{Edd} and the mass of the central black hole (M_{BH}). We note that the external Compton emission by NIR/optical/UV photons emitted by disk and dusty torus based clouds irradiated by a spine-sheath jet could in some cases be important (Finke 2016; Breiding et al. 2018; Gaur et al. 2018). Due to a lack of observational evidence, we do not include a dusty torus as a target photon field in our model.

Table 5
Results of Fitting Multiwavelength SEDs in Figure 7

Activity	Parameters	Symbol	Values	Activity period (days)
	Min Lorentz factor of injected electrons	γ_{min}	3.5	
	Max Lorentz factor of injected electrons	γ_{max}	7.5×10^3	
	BLR temperature	T'_{blr}	5×10^4 K	
	BLR photon density	U'_{blr}	1 erg cm^{-3}	
	Disk temperature	T'_{disk}	2.6×10^6 K	
	Disk photon density	U'_{disk}	3.7×10^{-7} erg cm^{-3}	
	Size of the emission region	R	6.5×10^{16} cm	
	Doppler factor of emission region	δ	35	
	Lorentz factor of emission region	Γ	15	
Preflare				
	Spectral index of injected electron spectrum (LP)	α	1.9	
	Curvature parameter of LP electron spectrum	β	0.08	
	Magnetic field in emission region	B	4.0 G	56
	Luminosity in injected electrons	L_e	1.78×10^{42} erg s^{-1}	
Rising				
	Spectral index of injected electron spectrum (LP)	α	1.8	
	Curvature parameter of LP electron spectrum	β	0.08	
	Magnetic field in emission region	B	4.1 G	29
	Luminosity in injected electrons	L_e	6.94×10^{42} erg s^{-1}	
Decaying				
	Spectral index of injected electron spectrum (LP)	α	1.8	
	Curvature parameter of LP electron spectrum	β	0.08	
	Magnetic field in emission region	B	4.1 G	22
	Luminosity in injected electrons	L_e	8.76×10^{42} erg s^{-1}	
Flare-1				
	Spectral index of injected electron spectrum (LP)	α	1.7	
	Curvature parameter of LP electron spectrum	β	0.02	
	Magnetic field in emission region	B	4.2 G	5
	Luminosity in injected electrons	L_e	1.27×10^{44} erg s^{-1}	
Flare-2				
	Spectral index of injected electron spectrum (LP)	α	1.7	
	Curvature parameter of LP electron spectrum	β	0.02	
	Magnetic field in emission region	B	4.1 G	8
	Luminosity in injected electrons	L_e	5.0×10^{43} erg s^{-1}	
Flare-3				
	Spectral index of injected electron spectrum (LP)	α	1.7	
	Curvature parameter of LP electron spectrum	β	0.02	
	Magnetic field in emission region	B	4.2 G	8
	Luminosity in injected electrons	L_e	9.04×10^{43} erg s^{-1}	
Flare-4				
	Spectral index of injected electron spectrum (LP)	α	1.7	
	Curvature parameter of LP electron spectrum	β	0.02	
	Magnetic field in emission region	B	4.2 G	7
	Luminosity in injected electrons	L_e	8.91×10^{43} erg s^{-1}	

Note. A LogParabola model is used as the electron injected spectrum, which is defined as $dN/dE = N_0(E/E_0)^{(-\alpha - \beta * \log(E/E_0))}$, where E_0 is chosen as 90 MeV.

The model's parameters are the magnetic field inside the blob, the Doppler factor of the blob, the spectral indices of the injected electron spectrum, and the luminosity of the injected electrons, whose values are optimized to fit the SEDs in Figure 7.

3.8. Multiwavelength SEDs

Time dependent multiwavelength modeling has been done with Swift UV, X-ray and *Fermi*-LAT γ-ray data for the preflare, rising segment, four flares and decaying segment.

In each phase the injected electron spectrum evolves with time as the electrons lose energy radiatively. The time evolution of the electron spectra is shown in right-hand panel of Figure 7. The Doppler factor is assumed to be 35, which is high compared to the values estimated by Casadio et al. (2015), and the Lorentz factor is 15. The size of the emission region is adjusted to 6.5×10^{16} cm to ensure that the SSC emission is not too high. In Figure 7, the X-ray data constrains the SSC emission. We note that intranight variability observed in optical flux suggests an upper limit on the size of the
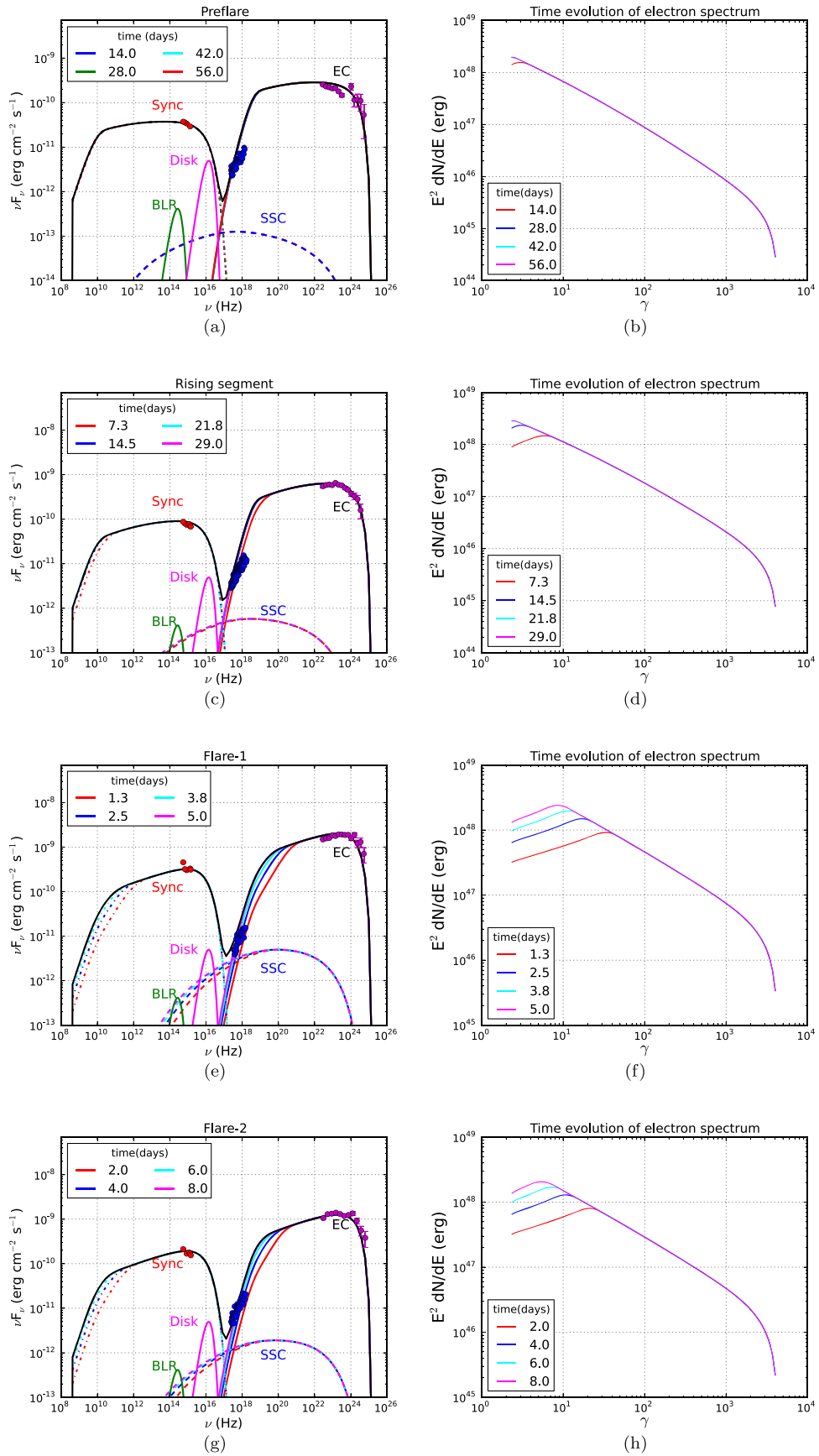
Figure 7. Modeled multiwavelength SEDs during different activity periods are shown in the left-hand panel. The plots are arranged in the following order preflare, rising segment, flare-1, flare-2, flare-3, flare-4 and decaying segment. Time evolution of electron spectra is shown in the right-hand panel. Each activity period is divided in four equal time intervals and shown in different colors. The model parameters are given in Table 5.
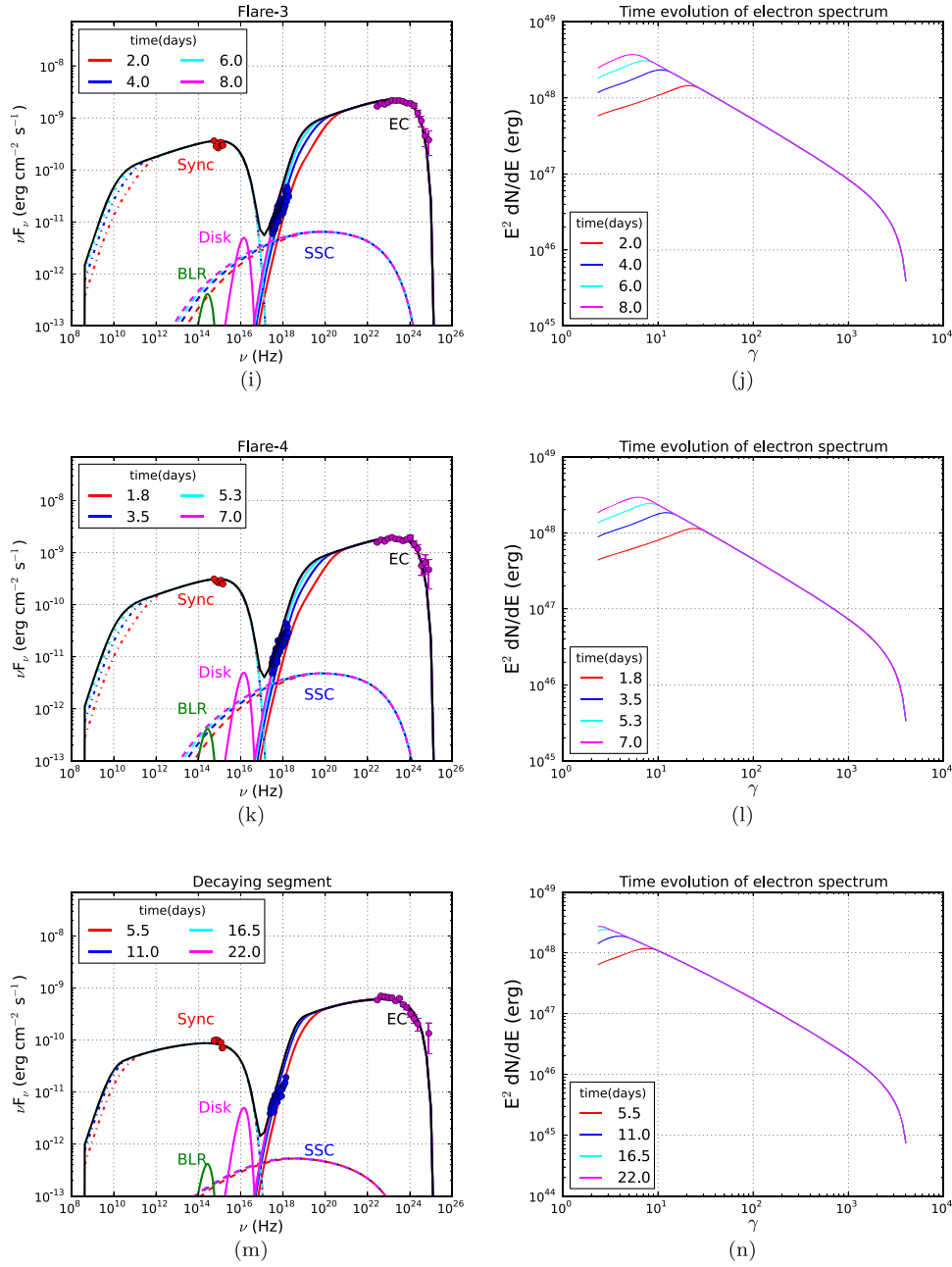
Figure 7. (Continued.)

emission region 4.5×10^{16} cm for Doppler factor 35, which is comparable to the size used in our model. In *Fermi*-LAT data, the variability time is observed to vary in the range of one hour to several days. The magnetic field rises from 4.0 to 4.2 G and the luminosity injected in electrons increases by nearly a factor of seventy as the source transits from the preflare to the flaring state. We also note that most of the jet power is in the magnetic field and not in the injected electrons. The maximum jet power required in our model is 6.6×10^{46} erg s^{-1}.

We have calculated the photon flux during each phase (preflare, rising segment, flare-1, flare-2, flare-3, flare-4 and decaying segment) and compared our results with the data in Figure 7. The values of the parameters, displayed in Table 5, are the best model parameters to fit the observed photon flux.

4. Discussion

The blazar CTA 102 was in active period during 2016 September–2017 March, not only in γ-ray but also in X-ray and optical/UV. In these 190 days, CTA 102 had four major γ-ray flares with the highest flux of 30.12 ± 4.48 (for 90 minutes binning). CTA 102 was also very bright in X-ray and optical/UV. All the γ-ray flares were simultaneous with the flares in X-ray and optical/UV, as shown in Figure 1.

The time evolution of the SEDs are shown in Figure 7.

Analysis of *Fermi*-LAT data shows variability in gamma-ray data in timescales of an hour to several days. Intranight variability has been observed in the optical flux (Bachev et al. 2017). For Doppler factor 35 intranight variability timescale gives an upper limit of 4.5×10^{16} cm on the size of the emission region. We have used 6.5×10^{16} cm in our work to ensure that the SSC

emission is not too high. The region size is related to the Doppler factor and variability timescale as

$$R \leqslant c \, t_{\text{var}} \, \delta (1 + z)^{-1}. \tag{12}$$

It is important to note that this relation is an approximation and there are other effects that may introduce large errors in determining the size of the emission region (Protheroe 2002).

We note that there could also be an EC emission from the target photons in the dusty torus region; however, due to the lack of observational information, we do not include the dusty torus region in our model.

The values of the parameters fitted in our multiwavelength modeling are shown in Table 5.

The rise in injected luminosity of electrons or jet power causing the rise in multiwavelength emission from the jet of CTA 102 during the flaring state can be explained by an increase in the accretion rate of the super massive black hole that powers the jet. The relationship between jet power and accretion in blazars has been well studied earlier. A large sample of blazars was used to study the jet-disc connection by Sbarrato et al. (2014), who noted that BLR luminosity is a tracer of accretion rate while gamma-ray luminosity is a tracer of jet power. It was also found that the two luminosities are linearly connected.

Fluctuation in luminosity and variability in an AGN was discussed as a stochastic process in Kelly et al. (2011), who gave a relationship between the characteristic timescale of high frequency X-ray emission and the black hole mass of an AGN.

Variability in blazar emission on timescales of days to years due to change in accretion rate was also discussed by Sartori et al. (2018), who modeled AGN variability as a result of variations in fueling of super massive black hole following the idea of Kelly et al. (2011). Unsteady fueling of black hole may occur due to physical processes of different spatial scales. Disc properties, such as its structure, viscosity and the system's response to perturbations could be among the factors influencing the conversion of gravitational energy to jet luminosity (Shakura & Sunyaev 1973).

Possible accretion disk origin of variability in jet of Mrk 421, which is a BL Lac, has been reported by Chatterjee et al. (2018). This source has a weak disc emission and strong jet emission in X-rays and showed a break in power spectral density, which could be connected to variation in accretion rate. This strengthens the motivation for the accretion-jet scenario of blazar flares.

Here, we discuss the other models that were considered earlier to explain flares of CTA 102. The evolution of physical parameters during the historical radio outburst in 2006 April was studied with a shock-in-jet model (Marscher & Gear 1985) by Fromm et al. (2011). In this model, a traveling shock wave evolves in a steady state jet. During the passage of the shock through the jet, the relativistic electrons carried down by the shock front get energy while crossing the shock front. Accelerated electrons cool down within a small layer behind the shock front. Magnetic field, Doppler factor, spectral index of electron spectrum and its normalization constant, and also the region size evolve as a PL in distance along the jet. Dominant loss energy mechanism of electrons was Compton during the first stage of the flare and adiabatic during the final stage. These authors concluded that a change in the evolution of the Doppler factor cannot explain the observed temporal evolution of the turnover frequency and turnover flux density.

Instead, they suggested that a shock-shock interaction (Fromm et al. 2013a) between traveling and standing shock wave might be the possible mechanism because it provides a better understanding of the evolution of the physical parameters compared to the shock-in-jet model.

Fromm et al. (2013a) found that the variability Doppler factor decreases from 17 in region C to 8 in region D with distance along the jet. At the same time, apparent speed decreases and the viewing angle increases. The deceleration of plasma flow along the jet was inferred from their analysis. The stationary behavior near $r \sim 1.5$ mas could arise from a recollimation shock at that position. The increase in viewing angle from region C to region D could be caused by helical instabilities due to asymmetric pressure in the jet.

In 2012 September–October, an exceptional outburst of CTA 102 was recorded (Larionov et al. 2016). The multiwavelength data covering NIR to gamma-ray frequencies was modeled by assuming that a radiating blob or shock wave moves along a helical path down the jet. The changes in the viewing angle caused by the motion of a shock wave along the helical path down the jet implied large changes in the value of the Doppler factor from 28 to 16. These authors inferred co-spatiality of optical and gamma-ray emission regions, which supports SSC mechanism of emission.

The gamma-ray flare of 2016 January was studied by a helical jet model by Li et al. (2018), who inferred a Doppler factor of 17.5 and size of the emission region 0.11–0.32 pc. They further inferred that the emission region is located at a distance of 5.7–16.7 pc from the central engine assuming a conical jet geometry. At a distance of 1 pc along the jet, they estimated a magnetic field 1.57 G using the core shift method.

In the paper by Zacharias et al. (2017), the flare of CTA 102 in 2016 and 2017 has been modeled by ablation of a gas cloud by a relativistic jet. The authors have assumed that a gradual increase in the number of injected electrons in the jet during the flare is due to slice by slice ablation of the cloud, until the center of the cloud is reached. Subsequently, the particle injection decreases, which results in decay of the flare. The value of the Doppler factor and BLR temperature used in our model is similar to Zacharias et al. (2017), who have assumed a magnetic field 3.7 G, which is comparable to the value assumed in our work. The region size is smaller 2.5×10^{16} cm in their model. The authors have assumed time dependent luminosity and spectral index of injected electrons. In our case, these variables are constants and adjusted for each state to obtain good fit to the data. In their model, EC by BLR photons is the main radiative loss mechanism of relativistic electrons and SSC emission is always insignificant.

The multiwavelength emission from CTA 102 has also been analyzed by Gasparyan et al. (2018), who have considered very short periods or time intervals of observation and the data is fitted with SSC and EC by BLR and torus photons. They noted spectral curvature and hardening in the gamma-ray spectra. In their work, the magnetic field and the luminosity in injected electrons differ significantly from one epoch to another epoch. Thus, the high activity states of CTA 102 have been analyzed and modeled earlier in different ways to obtain a good fit to the observed data and the variations in the values of the physical parameters (magnetic field, luminosity in injected electrons) are model dependent.

A study of the time evolution of the physical parameters (e.g., magnetic field, Doppler factor, spectral index and

luminosity in electrons, region size) required for SED modeling in preflare, flare and decaying states is necessary because the variations in the values of these parameters could be good indicators of the underlying model. At least some of the models could be excluded in this way. Simulated SEDs could be compared with the parametric fitting of SEDs for this purpose.

5. Concluding Remarks

We have studied the brightest flaring state of CTA 102, which was observed during 2016 September–2017 March. Four major flares have been identified between MJD 57735–57763 in γ-ray. Similar flares have also been observed in X-rays and optical/UV frequencies during this period. The preflare, rising phase before the four consecutive flares, the four major flares and the decay phase at the end have all been analyzed by spectral analysis of gamma-ray data and multi-wavelength SED modeling. The highest energy photon detected during the flaring episode is ∼73 GeV. The multi-wavelength data has been modeled using the time dependent code GAMERA to estimate the synchrotron and inverse Compton emission. Our study shows that the data can be fitted by a single zone model during various phases by varying the luminosity in injected electrons, and by slightly changing their spectral index and the magnetic field.

ORCID iDs

Raj Prince ⓘ https://orcid.org/0000-0002-1173-7310

References

Abdo, A. A., Ackermann, M., Ajello, M., et al. 2009, ApJS, 183, 46
Abdo, A. A., Ackermann, M., Ajello, M., et al. 2010a, ApJ, 710, 1271
Abdo, A. A., Ackermann, M., Ajello, M., et al. 2010b, ApJ, 188, 405
Abdo, A. A., Ackermann, M., Ajello, M., et al. 2010c, ApJ, 722, 520
Abdo, A. A., Ackermann, M., Ajello, M., et al. 2011, ApJL, 733, L26
Acero, F., Ackermann, M., Ajello, M., et al. 2015, ApJS, 218, 23
Ackermann, M., Ajello, M., Baldini, L., et al. 2010, ApJ, 721, 1383
Atwood, W. B., Abdo, A. A., Ackermann, M., et al. 2009, ApJ, 697, 1071
Bachev, R., Popov, V., Strigachev, A., et al. 2017, MNRAS, 471, 2216
Blandford, R. D., & Königl, A. 1979, ApJ, 232, 34
Blumenthal, R., & Gould, G. 1970, RvMP, 42, 237
Bonning, E. W., Bailyn, C., Urry, C. M., et al. 2009, ApJL, 697, L81
Breeveld, A. A., Landsman, W., Holland, S. T., et al. 2011, in AIP Conf. Ser. 1358, Gamma Ray Bursts, ed. J. E. McEnery, J. L. Racusin, & N. Gehrels (Melville, NY: AIP), 373
Breiding, P., Georganpoulos, M., & Meyer, E. 2018, ApJ, 853, 19
Britto, R. J. G., Bottacini, E., Lott, B., et al. 2016, ApJ, 830, 162
Casadio, C., Gomez, J. L., Jorstad, S. G., et al. 2015, ApJ, 813, 51
Chatterjee, R., Bailyn, C. D., Bonning, E. W., et al. 2012, ApJ, 749, 191
Chatterjee, R., Roychowdhury, A., Chandra, S., & Sinha, A. 2018, ApJL, 859, L21
Chiaberge, M., & Ghisellini, G. 1999, MNRAS, 306, 551
Dermer, C. D., & Menon, G. 2009, High Energy Radiation from Black Holes (Princeton, NJ: Princeton Univ. Press)
Edelson, R. A., Krolik, J. H., & Pike, G. F. 1990, ApJ, 359, 86
Edelson, R. A., & Malkan, M. A. 1987, ApJ, 323, 516
Finke, J. 2016, ApJ, 830, 94
Fromm, C. M., Perucho, M., Ros, E., et al. 2011, A&A, 531, A95
Fromm, C. M., Ros, E., Perucho, M., et al. 2013a, A & A, 551, A32
Fromm, C. M., Ros, E., Perucho, M., et al. 2013b, A&A, 557, A105
Gasparyan, S., Sahakyan, N., Baghmanyan, V., & Zargaryan, D. 2018, ApJ, 863, 114
Gaur, H., Mohan, P., Wiercholska, A., & Gu, M. 2018, MNRAS, 473, 3638
Hahn, J. 2015, Proc. ICRC, 34, 917
Jorstad, S. G., Marscher, A. P., Lister, A. P., et al. 2005, AJ, 130, 1418
Jorstad, S. G., Marscher, A. P., Mattox, J. R., et al. 2001, ApJS, 134, 181
Kalberla, P. M. W., Burton, W. B., Hartmann, D., et al. 2005, A&A, 440, 775
Kaur, N., & Baliyan, K. S. 2018, A&A, in press (arXiv:1805.04692)
Kelly, B. C., Sobolewska, M., & Siemiginowska, A. 2011, ApJ, 730, 52
Larionov, V. M., Villata, M., Raiteri, C. M., et al. 2016, MNRAS, 461, 3047
Li, X., Mohan, P., An, T., et al. 2018, ApJ, 854, 17
Lister, M. L., Aller, M. F., Aller, H. D., Homan, D. C., et al. 2013, AJ, 146, 120
Maraschi, L., Ghisellini, G., Tanzi, E. G., & Treves, A. 1986, ApJ, 310, 325
Marscher, A. P., & Gear, W. K. 1985, ApJ, 298, 114
Massaro, E., Perri, M., Giomi, P., & Nesci, R. 2004, A &A, 413, 489
Mattox, J. R., Bertsch, D. L., Chiang, J., et al. 1996, ApJ, 461, 396
Moore, R. L., & Stockman, H. S. 1981, ApJ, 243, 60
Nolan, P. L., Abdo, A. A., Ackermann, M., et al. 2012, ApJS, 119, 31
Nolan, P. L., Bertsch, D. L., Fichtel, C. E., et al. 1993, ApJ, 414, 82
Osterman Meyer, A., Miller, H. R., Marshall, K., et al. 2009, AJ, 138, 1902
Paliya, V. S. 2015, ApJL, 808, L48
Paliya, V. S., Sahayanathan, S., & Stalin, C. S. 2015, ApJ, 803, 15
Patel, S. R., Shukla, A., Chitnis, V. R., et al. 2018, A&A, 611, A44
Pian, E., Falomo, R., & Treves, A. 2005, MNRAS, 361, 919
Prince, R., Majumdar, P., & Gupta, N. 2017, ApJ, 844, 62
Protheroe, R. J. 2002, PASA, 19, 486
Roming, P. W. A., Kennedy, T. E., Mason, K. O., et al. 2005, SSRv, 120, 95
Sandage, A., & Wyndham, J. D. 1965, ApJ, 141, 328
Sartori, L. F., Schawinski, K., Trakhtenbrot, B., et al. 2018, MNRAS, 476L, 34
Sbarrato, T., Padovani, P., & Ghisellini, G. 2014, MNRAS, 445, 81
Schlafly, E. F., & Finkbeiner, D. P. 2011, ApJ, 737, 103
Schmidt, M. 1965, ApJ, 141, 1295
Shakura, N. I., & Sunyaev, R. A. 1973, A&A, 24, 337
Spencer, R. E., McDowell, J. C., Charlesworth, M., et al. 1989, MNRAS, 240, 657
Stanghellini, C., O'Dea, C. P., Dallacasa, D., et al. 1998, A&AS, 131, 303
Vaughan, S., Edelson, R., Warwick, R. S., & Uttley, P. 2003, MNRAS, 345, 1271
Zacharias, M., Böttcher, M., Jankowsky, F., et al. 2017, ApJ, 851, 72
Zamaninasab, M., Clausen-Brown, E., Savolainen, T., & Tchekhovskoy, A. 2014, Natur, 510, 126